Sub-ppm H_2S sensing by tubular ZnO-Co_3O_4 nanofibers

M.N. Rumyantseva[a,*], S.A. Vladimirova[a], V.B. Platonov[a], A.S. Chizhov[a], M. Batuk[b], J. Hadermann[b], N.O. Khmelevsky[c], A.M. Gaskov[a]

[a] Chemistry Department, Moscow State University, 119991, Moscow, Russia
[b] EMAT, University of Antwerp, B-2020, Antwerp, Belgium
[c] LISM, Moscow State Technological University Stankin, 127055, Moscow, Russia

A B S T R A C T

Tubular ZnO – Co_3O_4 nanofibers were co-electrospun from polymer solution containing zinc and cobalt acetates. Phase composition, cobalt electronic state and element distribution in the fibers were investigated by XRD, SEM, HRTEM, HAADF-STEM with EDX mapping, and XPS. Bare ZnO has high selective sensitivity to NO and NO_2, while ZnO-Co_3O_4 composites demonstrate selective sensitivity to H_2S in dry and humid air. This effect is dis-cussed in terms of transformation of cobalt oxides into cobalt sulfides and change in the acidity of ZnO oxide surface upon cobalt doping. Reduction in response and recovery time is attributed to the formation of a tubular structure facilitating gas transport through the sensitive layer.

1. Introduction

Creation of composite materials combining metal oxides of different reactivity is used to improve the performances of semiconductor gas sensors [1–3]. The nanocomposites including *p*-type M1O: NiO, CuO, Co_3O_4 and *n*-type M2O: ZnO, SnO_2, WO_3, In_2O_3, semiconductor oxides are of particular interest. As compared with individual oxides the electrical conductivity of M1O-M2O composites exhibits higher sensitivity to the surrounding atmosphere, since the gas adsorption affects the barrier height at the *p* - *n* heterojunction [4–10].

In recent years, a considerable attention is paid to the ZnO-Co_3O_4 nanocomposites [11–21]. These oxides complement each other in sensor activity. ZnO is a wide-gap *n*-type semiconductor (E_g = 3.4 eV) widely used as a material for solar cells [22], LED [23], lasing [24], fluorescence imaging [25] and for gas sensors [26]. Among *p*-type semiconductor oxides studied as materials for gas sensors [27], Co_3O_4, is one of the most active catalysts for the oxidation processes [28,29]. Most of the works on the gas sensor properties of ZnO-Co_3O_4 nanocomposites is devoted to the detection of volatile organic compounds (VOCs) [12–16,18,12–21]. At the same time, sensor characteristics of ZnO-Co_3O_4 nanocomposites to main air pollutants CO, NH_3, H_2S have not been studied.

In the present work, ZnO-Co_3O_4 nanocomposites and individual oxides *n*-ZnO and *p*-Co_3O_4 were obtained by electrospinning. This is an inexpensive tool, widely used for preparation of one-dimensional (1D) nanofibers, including ZnO-Co_3O_4 nanocomposites [11,17,18]. The combination of unlimited length, highly porous structure and high surface area of nanofibers is important for application in catalysis and chemical sensing [30–33].

The work is aimed at studying the effect of [Co]/[Zn] ratio on morphology and gas sensor properties of composite nanofibers toward main air pollutants, NO, NO_2, NH_3, CO, H_2S in dry (relative humidity at 25 °C RH_{25} = 0 %) and humid (RH_{25} = 60 %) air.

2. Experimental

2.1. Preparation

The synthesis scheme is illustrated in Fig. S1 (Supplementary Material). $Zn(CH_3COO)_2$ $2H_2O$ and $Co(CH_3COO)_2$ $4H_2O$ were dissolved in a mixture of 2-methoxyethanol and isopropanol. After stirring for 30 min at room temperature (RT), polyvinylpyrrolidone (PVP) was added to the solution with stirring for 3 h. Co-electrospinning was performed under 11 kV, the distance between the syringe needle and collector was 13 cm. The solution flow of 1 ml/h was controlled by a syringe pump. The obtained polymer nanofibers were collected and dried in air. The annealing conditions for polymer decomposition (550 °C, 5 h) were determined by thermogravimetric analysis with mass spectral analysis of gaseous products (TG-MS) using a NETZSCH STA 409 PC/PG instrument.

* Corresponding author.
E-mail address: roum@inorg.chem.msu.ru (M.N. Rumyantseva).

Table 1
Composition and crystal structure parameters of ZnO-Co_3O_4 nanofibers.

Sample	[Co]/([Co] + [Zn]) (wt.%)	Phase composition	Parameters of wurtzite phase		
			a, Å	*c*, Å	d_{XRD}, nm
ZnO	0	ZnO	3.2475(8)	5.1953(5)	10 ± 1
ZnCo7	6.5 ± 0.3	$Zn_{1-y}Co_yO$	3.2477(16)	5.208(3)	12 ± 1
ZnCo13	13.4 ± 0.7	$Zn_{1-y}Co_yO$ + $Zn_xCo_{3-x}O_4$	3.2450(4)	5.199(1)	14 ± 2
ZnCo22	22 ± 1	$Zn_{1-y}Co_yO$ + $Zn_xCo_{3-x}O_4$	3.2416(25)	5.189(5)	13 ± 2
ZnCo30	30 ± 2	$Zn_{1-y}Co_yO$ + $Zn_xCo_{3-x}O_4$	3.2461(7)	5.196(1)	16 ± 2
Co_3O_4	100	Co_3O_4	–	–	–

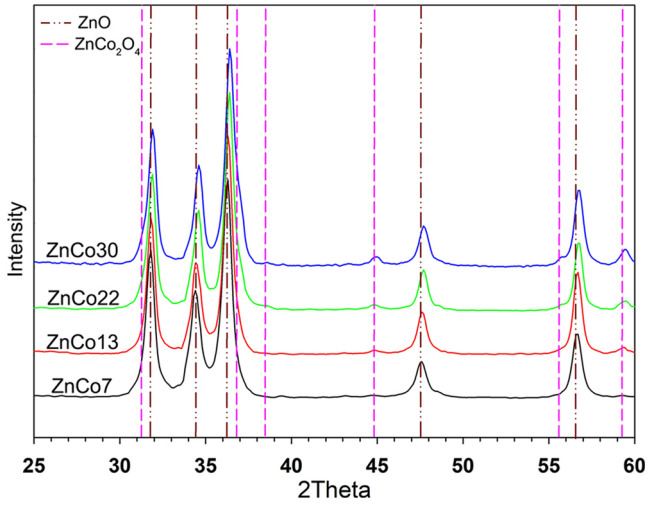

Fig. 1. X-ray diffraction patterns of the ZnO-Co_3O_4 composite nanofibers. Dash and dash-dot lines correspond to the reflection positions of $ZnCo_2O_4$ (ICDD 23–1390) and ZnO (ICDD 36–1451), respectively.

2.2. Characterization and measurement

The composition of ZnO-Co_3O_4 nanofibers was determined by X-ray fluorescence analysis (XRF) using a M1 Mistral (Bruker) spectrometer previously calibrated by inductively coupled plasma mass spectrometry (ICP-MS) (Agilent 7500C). The phase composition was determined by X-ray diffraction (XRD) method using a DRON-4 M diffractometer (Cu Kα, λ = 1.5406). The crystallite size (d_{XRD}) of ZnO and Co_3O_4 phases in nanofibers was estimated using the Scherrer formula. The specific surface area was measured by the low-temperature nitrogen adsorption using a Chemisorb 2750 (Micromeritics). The morphology of the nanofibers was studied by scanning electron microscopy (SEM) using a Carl Zeiss NVision 40 electron microscope at 5 kV. The microstructure of the samples and elements distribution were investigated using high resolution transmission electron microscopy (HRTEM), high angle annular dark field scanning transmission electron microscopy (HAADF-STEM), and energy dispersive X-ray (EDX) mapping on a FEI Osiris microscope equipped with a Super-X detector operated at 200 kV. X-ray photoelectron spectra (XPS) were registered with Axis Ultra DLD (Kratos, UK) spectrometer with Al K_α source; binding energy was calibrated by C 1s signal at 285.0 eV.

Gas sensor tests were performed by *in situ* conductivity measurements in an automatic set up with a flow chamber. The oxide nanofibers were ground with α-terpineol to obtain a paste. The sensors were then fabricated *via* drop-deposition of the paste onto alumina microhotplates provided with vapor-deposited Pt electrodes (0.3 mm × 0.2 mm separated by 0.2 mm gap) and with embedded Pt-meanders. The paste was dried at RT and then calcined at 250°C in purified air for 20 h. The sensing layer formed was about 1 mm × 0.5 mm in dimensions with the thickness of 5–7 μm. The sensor resistance was measured at 1.3 V DC-voltage under controlled gas flow of 100 ± 0.1 mL/min at a temperature fixed in the range of 80–300 °C. The test gases were NO (4 ppm), NO_2 (1 ppm), NH_3 (20 ppm), CO (20 ppm) and H_2S (0.2–2 ppm) in purified air created by the dilution of certified gas mixtures. To create gas mixtures with a pre-assigned oxygen content the commercially available Ar (no more than 0.002 vol. % O_2) and synthetic air (20 vol. % O_2) were used. The gas concentrations and flows were controlled by EL-FLOW mass-flow controllers (Bronkhorst). The humidity was set and controlled by P-2 Cellkraft humidifier.

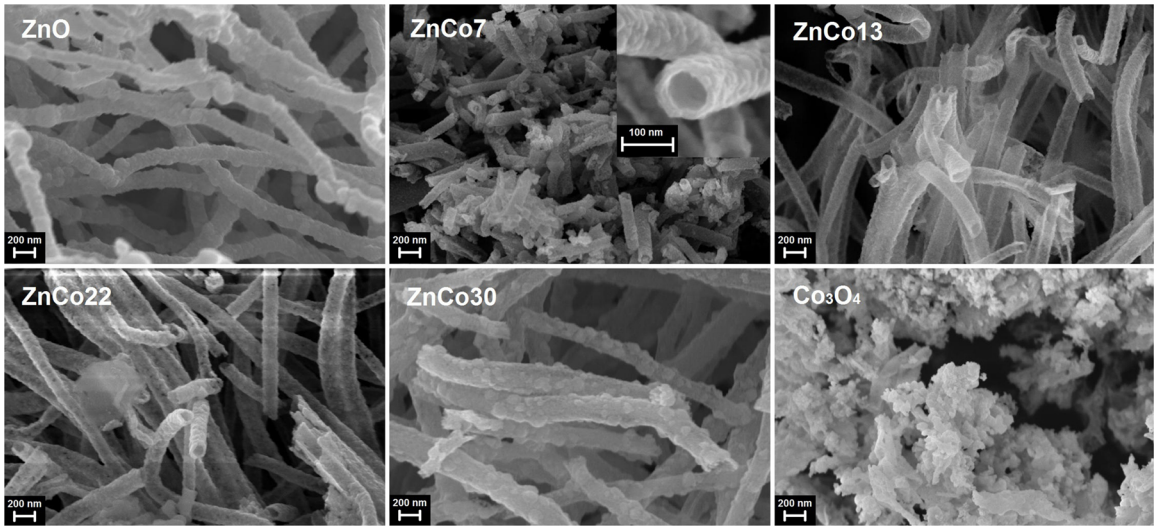

Fig. 2. SEM images of ZnO-Co_3O_4 composite nanofibers.

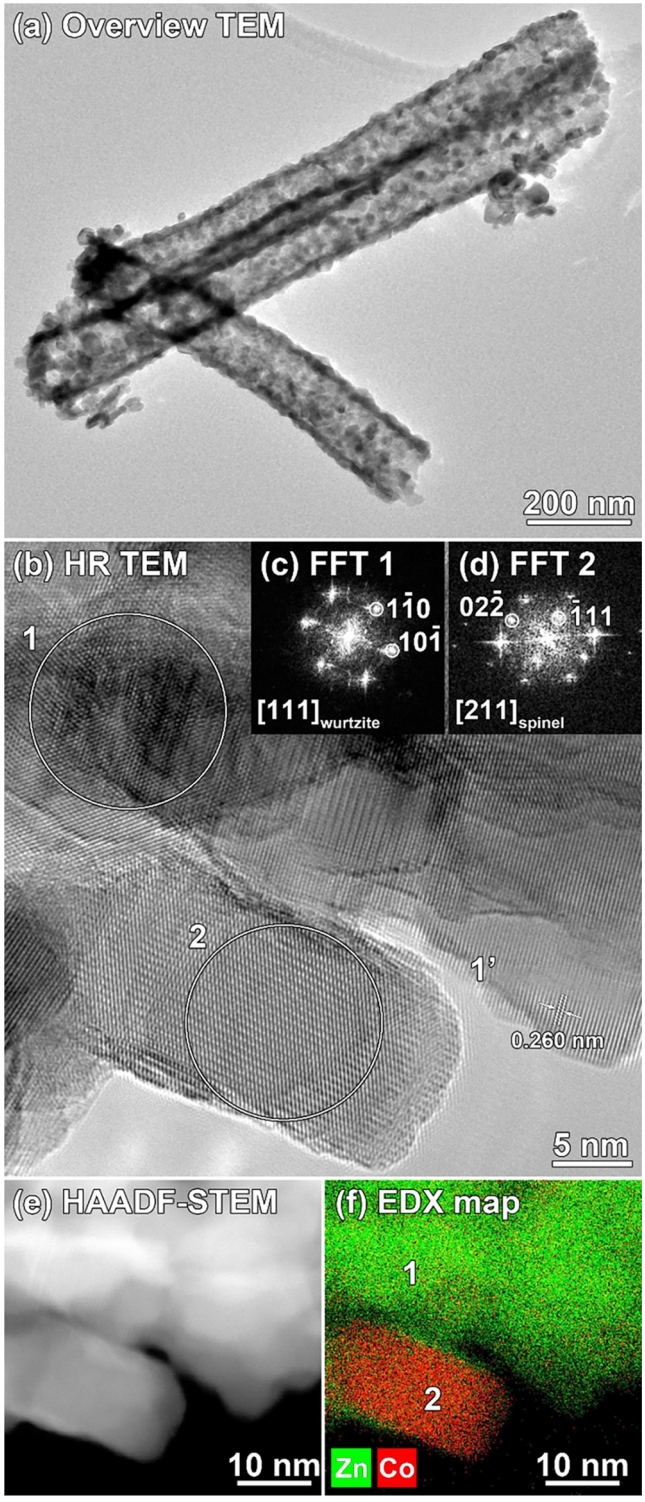

Fig. 3. Low magnification (a) and high resolution (b) TEM images of the ZnCo13 sample; fast Fourier transform (FFT) taken from the circled regions 1 (c) and 2 (d); HAADF-STEM image (e) and corresponding STEM-EDX mixed Zn/Co map (f). The STEM-EDX map reveals regions enriched with zinc (5 at. % Co, region 1) and cobalt (61 at. % Co, region 2).

3. Results and discussion

The list of synthesized samples, their composition and microstructure parameters are given in Table 1. According to XRD the samples prepared from zinc acetate solution and from solution of low cobalt content (ZnCo7) contain only one crystalline phase ZnO wurtzite (Fig. 1). An increase of cobalt concentration leads to the appearance of the phase with the spinel structure. The exact composition of this phase cannot be determined from XRD because of the close arrangement of the reflections corresponding to Co_3O_4 (ICDD 42–1467), $ZnCo_2O_4$ (ICDD 23–1390) and solid solutions $Zn_xCo_{3-x}O_4$ (ICDD from No. 81-2295 to No. 81-2299). Since the most intense reflections of spinel $Zn_xCo_{3-x}O_4$ phase ($d_{220}(Co_3O_4)$ = 2.8580 Å, $d_{220}(ZnCo_2O_4)$ = 2.8630 Å; $d_{311}(Co_3O_4)$ = 2.4370 Å, $d_{311}(ZnCo_2O_4)$ = 2.4400 Å) overlap with the intense diffraction maxima of wurtzite ZnO (ICDD 36–1451, d_{100}(ZnO) = 2.8143 Å, d_{101}(ZnO) = 2.4759 Å), and because of the low concentration of the spinel crystalline phase in the samples, the determination of the unit cell parameters of $Zn_xCo_{3-x}O_4$ is impossible. The unit cell parameters *a* and *c* of the wurtzite phase change with the increase in the cobalt content in the nanofibers (Table 1). This can indicate the formation of a $Zn_{1-y}Co_yO$ solid solutions. However, the change in parameters is small and does not allow to reveal an unambiguous relationship between the concentration of cobalt in the nanofibers and the composition of the solid solution $Zn_{1-y}Co_yO$. The crystallite size d_{XRD} for pure ZnO was 10 ± 2 nm, for pure cobalt oxide Co_3O_4 14 ± 2 nm, and for solid solutions $Zn_{1-y}Co_yO$ d_{XRD} increases from 12 to 16 nm with cobalt concentration.

In general, electrospinning allows producing porous nanotubes with extremely large aspect ratios [34]. The nanofibers typically have a diameter range from a few ten nanometers to a few micrometers. In addition, it is possible to use this method to obtain nanofibers/ nanotubes, with specific surface topologies. Moreover, by extension of the coaxial spinneret system multishell nanostructures can be formed. Due to their high surface-to-volume ratio, such porous nanofibers appear to be more preferable for gas sensor application than single crystal nanorods obtained *via* hydrothermal route [35]. The evolution of nanofiber morphology with increasing cobalt concentration is shown in Fig. 2. Pure ZnO consists of randomly oriented long wires composed of ordered ZnO nanoparticles. The presence of cobalt leads to the formation of hollow tubes with an inner diameter of 80 − 100 nm. In the case of Co_3O_4 the fibers do not form. The tubular structure appears at the stage of post synthetic annealing. $Co(CH_3COO)_2$ decomposes earlier than $Zn(CH_3COO)_2$ (Supplementary Material, Fig. S2) and displaces to the surface of the fibers forming the outer wall of the nanotubes [34]. The specific surface area increases from 9 ± 1 m^2/g for ZnO nanofibers to 12 − 15 m^2/g for ZnO-Co_3O_4 composite nanofibers.

The low magnification TEM image of ZnCo13 (Fig. 3a) confirms the formation of tubular fibres consisting of agglomerated nanoparticles. HR TEM images (Fig. 3b) indicate that the nanotube wall is formed by nanoparticles of ZnO or $Zn_{1-y}Co_yO$ solid solution with low cobalt content. The Fourier transform (FT) acquired from region 1 (Fig. 3c) corresponds to the [111] direction of wurtzite structure and the interplanar distance in region 1′ is close to 0.260 nm, which corresponds to the (002) crystallographic planes in wurtzite. The FT of region 2 (Fig. 3d) can be indexed in the spinel structure Co_3O_4 or $ZnCo_2O_4$. According to the complementary STEM-EDX map from this area (Fig. 3e,f), the particles with a wurtzite structure ($Zn_{1-y}Co_yO$) have 5 at. % Co and the particle with a spinel structure has 61 at. % Co that corresponds to the composition close to $ZnCo_2O_4$ Therefore, it can be argued that as the cobalt content increases, nanoparticles with a spinel structure are formed on the surface of the nanofibers.

Low magnification HAADF-STEM image combined with STEM-EDX maps confirms the uneven distribution of cobalt along the surface of the ZnCo13 nanofibers (Fig. 4). The high magnification EDX maps of ZnCo13 (Fig. 5a,c) and ZnCo30 (Fig. 5b,d) nanocomposites reveals the particles enriched with zinc (1) and cobalt (2). The cobalt enriched particles contain 64 at.% Co (ZnCo13, Fig. 5c) and 84 at.% Co (ZnCo30, Fig. 5d), that correspond to $ZnCo_2O_4$ and $Zn_{0.5}Co_{2.5}O_4$, respectively. The zinc enriched areas contain about 5 at. % Co. In both cases, the concentration of cobalt in areas (2) exceeds the average value determined by the XRF method (Table 1). This set of the results allows us to conclude that the walls of the tubular structures are formed by

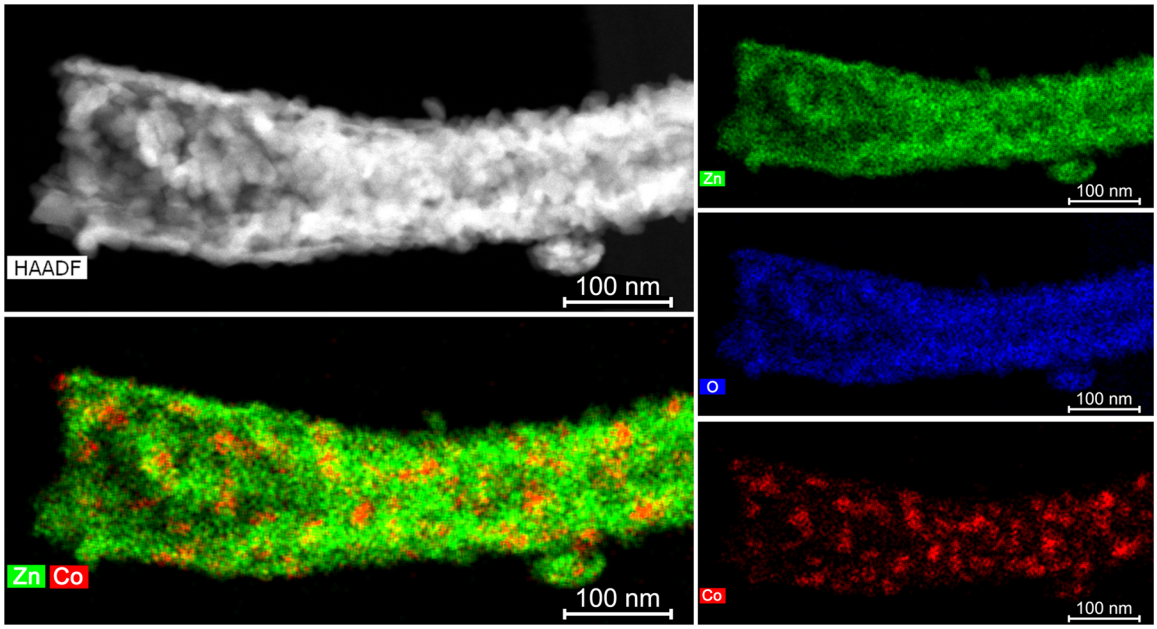

Fig. 4. HAADF-STEM image and STEM-EDX maps of ZnCo13 nanocomposite.

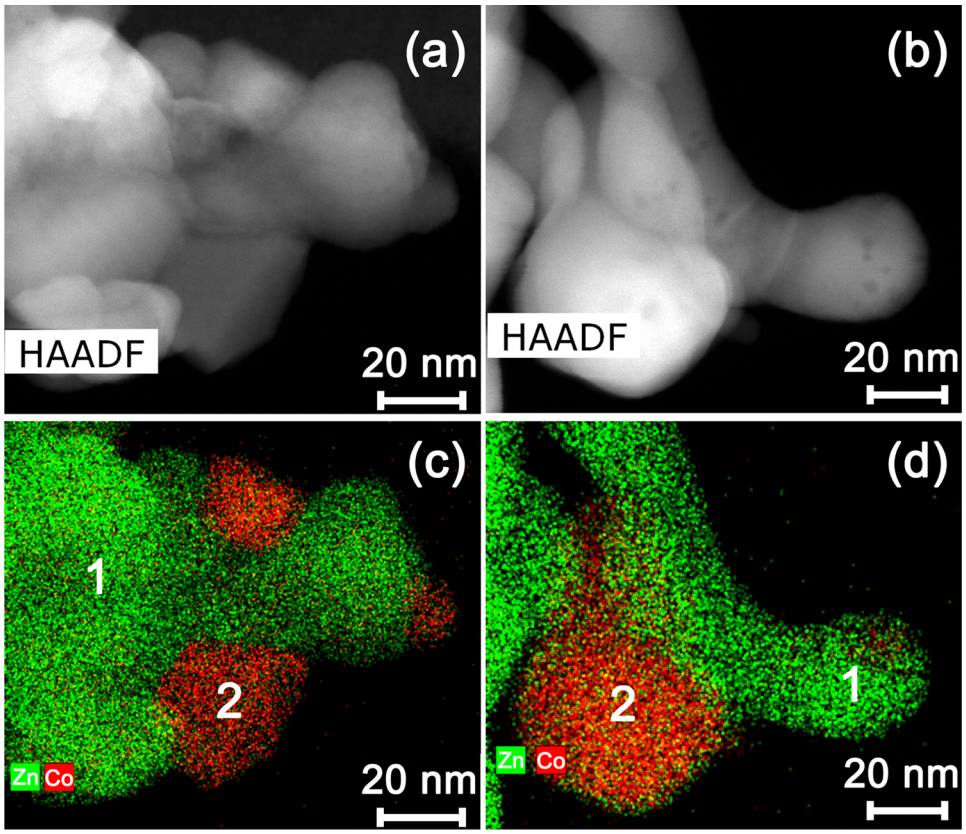

Fig. 5. HAADF-STEM images and STEM-EDX maps of ZnCo13 (a, c) and ZnCo30 (b, d) composite nanofibers. STEM-EDX maps revealed the areas enriched with zinc (1) and cobalt (2). The composition of cobalt enriched areas: 64 at. %Co (a) and 84 at. % Co (b); of zinc enriched areas: 5 at. % Co.

agglomerated nanoparticles of wurtzite $Zn_{1-y}Co_yO$ (y ≈ 0.05). Nanoparticles with higher cobalt content, spinel $Zn_xCo_{3-x}O_4$, are present on the surface of the wall. An increase in the total cobalt content in the nanocomposites leads to an increase in the cobalt concentration in spinel $Zn_xCo_{3-x}O_4$ solid solutions.

The Co2p X-ray photoelectron spectra of ZnCo7, ZnCo13, ZnCo30 and Co_3O_4 samples are presented in Fig. 6. In the ZnCo7 nanofibers cobalt is present only in Co^{2+} oxidation state (E = 780.8 eV). The peak position of the shake-up satellite (E = 786.0 eV) corresponds to the octahedral environment of Co^{2+}, which can be realized in interstitial positions in wurtzite $Zn_{1-y}Co_yO$ or in CoO oxide, which does not appear on the ZnCo7 diffractogram. An increase in the cobalt content results in the appearance of the Co^{3+} component (E = 779.7 eV), that is in agreement with the formation of the spinel phase. A further increase in

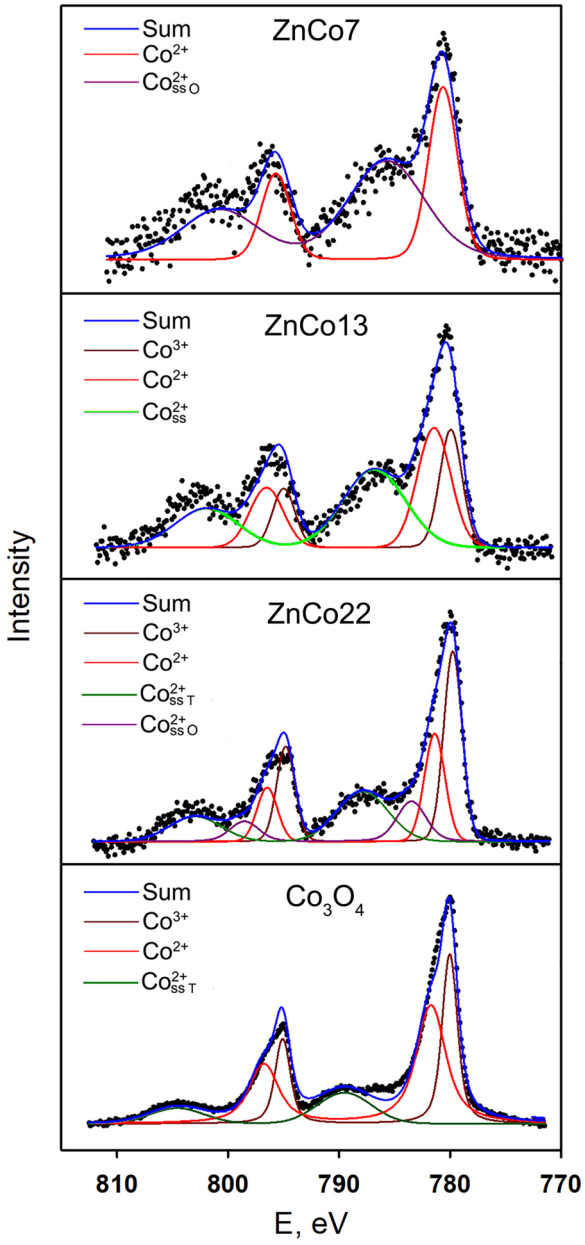

Fig. 6. Co 2p XP-spectra fitted by 2 or 4 doublets corresponding to Co(III) (dark red) and Co(II) (red) main peaks and Co(II) shake-up satellites, corresponding to tetrahedral (dark green) and octahedral (dark pink) coordination environment (For interpretation of the references to colour in this figure legend, the reader is referred to the web version of this article).

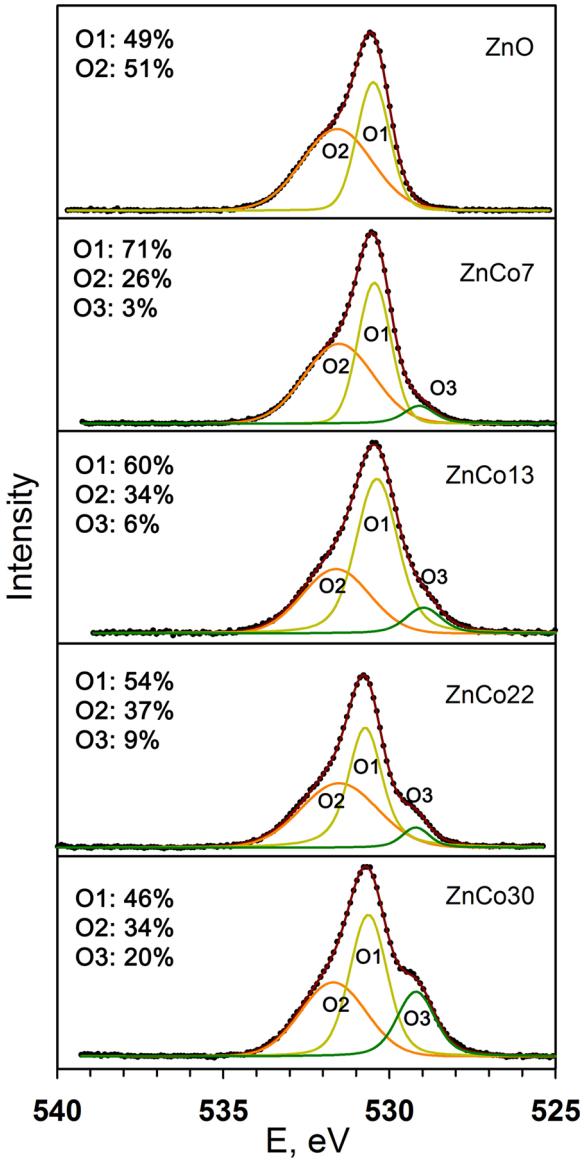

Fig. 7. O 1s XP-spectra of the ZnO and ZnO-Co_3O_4 nanofibers.

the cobalt content leads to an increase in the contribution of the Co^{3+} component and the appearance of two shake-up satellites corresponding to the Co^{2+} tetrahedral coordination in the spinel structure (E = 788.0 eV) and the octahedral environment in $Zn_{1-y}Co_yO$ or in CoO (E = 783.4 eV).

The O1 s XP-spectra of the ZnO nanofibers and nanocomposites are shown in Fig. 7. The O1 s spectrum of ZnO contains two components with maxima at 530.5 eV (O1) and 531.5 eV (O2). The O1 component corresponds to the lattice oxygen of ZnO, and the O2 component is related with the various oxygen-containing particles chemisorbed on the ZnO surface. The introduction of cobalt is accompanied by the appearance and growth of a third component (O3, E = 529.0 eV), which can be attributed to cobalt bound oxygen. At the same time, there is a sharp decrease in the amount of chemisorbed oxygen for ZnCo7 nanocomposite compared with unmodified ZnO: the ratio of integral intensities O2/O1 ≈ 1 for ZnO and O2/(O1 + O3) ≈ 0.4 for ZnCo7. In the O1 s spectra of ZnCo13, ZnCo22 and ZnCo30 nanocomposites, the contribution of chemisorbed oxygen is close within O2/(O1 + O3) = 0.5 – 0.6. So, a distribution of cobalt between $Zn_{1-y}Co_yO$ and $Zn_xCo_{3-x}O_4$ solid solutions is accompanied by a non-monotonic change in the concentration of chemisorbed oxygen on the surface of nanocomposites. In general, unlike Fe_2O_3/ZnO nanocomposites [36], the introduction of cobalt reduces the amount of oxygen chemisorbed on the surface of ZnO nanofibers.

For a more detailed study of the effect of cobalt on the interaction of ZnO with oxygen, the predominant form of chemisorbed oxygen on the surface of nanocomposites was evaluated from the dependence of the electrical conductivity of the samples on the partial pressure of oxygen. Oxygen adsorption on the surface of *n*-type semiconductor oxides occurs with electron localization

$$\frac{\beta}{2}\bullet O_{2(gas)} + \alpha\bullet e^- \leftrightarrow O^{\alpha-}_{\beta(ads)} \quad (1)$$

The authors [37] show that for a porous layer formed by *n*-type

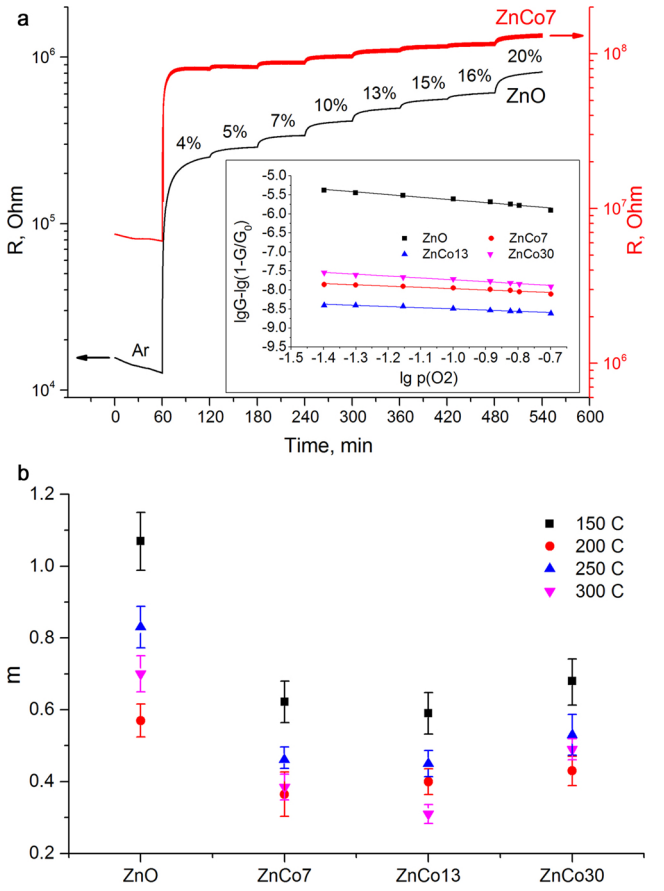

Fig. 8. (a) Resistance of unmodified ZnO and ZnCo7 nanocomposites *vs.* oxygen partial pressure at 250 °C. Inset: Dependencies of electrical conductivity of the samples on the oxygen partial pressure at 250 °C in coordinates $lg(G) - lg(1 - \frac{G}{G_0})$ *vs.* $lg(p_{O_2})$ corresponding to Eq. (2). (b) Coefficient *m* corresponding to the predominant chemisorbed oxygen species on the surface of ZnO and ZnO-Co_3O_4 nanofibers at different temperatures.

Table 2
Ionic-covalent parameter (ICP) of cations depending on oxygen environment [41].

Cation	ICP		
	Tetrahedral environment	Octahedral environment	
		High spin	Low spin
Zn^{2+}	0.718	0.596	
Co^{2+}	0.656	0.510	0.587
Co^{3+}	–	0.606	0.550

nanocrystalline semiconductors with crystallite size $d < 2w$ (w is a depletion layer width), the electrical conductivity G is linearly dependent on the oxygen partial pressure p_{O2} in logarithmic coordinates:

$$\lg G - \lg\left(1 - \frac{G}{G_0}\right) = const - m \cdot \lg(p_{O2}) \quad (2)$$

where G is the conductivity in the presence of oxygen, G_0 is the conductivity in inert atmosphere. Parameter $m = \beta/2\alpha$ corresponds to the form of chemisorbed oxygen. Depending on temperature, the predominant chemisorbed oxygen species are either molecular O_2^- (at 100–170 °C, $m = 1$), or atomic O^- (at 200–350 °C, $m = 0.5$) and O^{2-} (above 400 °C, $m = 0.25$) [38]. Since ZnO depletion layer width is about 15 nm [39,40] and ZnO crystallite size in nanocomposites d_{XRD} does not exceed 16 nm (Table 1), the condition $d < 2w$ is satisfied for all studied samples. The *in situ* conductivity measurements showed that with increasing oxygen content in the gas phase, the electrical resistance of materials increases (Fig. 8a). This behavior, typical for *n*-type semiconductor oxides, was registered for all studied samples at 150–300 °C. The dependence of electrical conductivity on the oxygen partial pressure are linear in coordinates corresponding to Eq. (2) (Fig. 8a, inset). The values of the coefficient *m* corresponding to the predominant type of chemisorbed oxygen calculated from the slope angle of these dependences are summarized in Fig. 8b. The following trends can be noted. At 150 °C on the surface of ZnO nanofibers, oxygen is adsorbed in molecular form O_2^-. An increase in temperature naturally leads to an increase in the proportion of the atomic form O^-. The introduction of cobalt leads to the further increase in the proportion of the atomic forms of chemisorbed oxygen O^- and even O^{2-} (at the same temperature). This indicates a decrease in surface acidity of nanocomposites compared to ZnO nanofibers. For example, in [3] it is shown that with a decrease in Lewis acidity of cations introduced into tin dioxide, the atomic forms of oxygen prevail over the molecular ones. Portier et al. [41] proposed a parameter related to acid strength of a cation that simultaneously characterizes the ionic and covalent contributions to the formation of the metal-oxygen bond in the oxide compound (ionic-covalent parameter, ICP). Based on the ICP values [41] (Table 2), it can be concluded that the substitution of Zn^{2+} in the wurtzite structure by Co^{2+} both in the tetrahedral lattice sites and in the octahedral interstitial positions (high spin (HS) state) leads to a decrease in the ZnO surface acidity. Cations Co^{3+} in the octahedral positions of the spinel structure are in the low-spin (LS) state and are characterized by lower acidity than Zn^{2+} in both tetrahedral and octahedral oxygen environments. Thus, the formation of both $Zn_{1-y}Co_yO$ and $Zn_xCo_{3-x}O_4$ solid solutions leads to a decrease in the acidity of the surface of nanocomposites compared with unmodified ZnO, that can provide the increase in the concentration of atomic forms of chemisorbed oxygen.

The sensor properties were measured by resistance transient on exposing to different air pollutants: NO, NO_2, NH_3, CO and H_2S in dry (RH_{25} = 0 %) and humid (RH_{25} = 60 %) conditions. The repeated response of ZnO, Co_3O_4, ZnCo7 and ZnCo13 nanofibers to NO_2 in dry air at different temperatures is shown in Fig. 9 as an example. Adding cobalt leads to a sharp increase in ZnO resistance (Fig. 9; Supplementary Material, Fig. S3) that may be caused by the formation of heterojunctions at the interfaces between different semiconductors (*n*-type $Zn_{1-y}Co_yO$ and *p*-type CoO_x or *p*-type $Zn_xCo_{3-x}O_4$ [10–21]). The sensor signal S was defined as the ratio of resistance R or conductivity G in air (R_{air}, G_{air}) and in the presence of the target gas (R_{gas}, G_{gas}):

$$S = \frac{G_{gas} - G_{air}}{G_{air}} \quad (3)$$

$$\text{or } S = \frac{R_{gas} - R_{air}}{R_{air}} \quad (4)$$

The comparison of sensor signals to NO, NO_2, NH_3, CO and H_2S at the temperatures corresponding to the maximum sensitivity to each gas is shown in Fig. 10 In both dry and humid air, the sensors activity of bare ZnO is superior in detecting NO_2 even at 80 °C, the introduction of cobalt leads to a decrease in the sensor signal. Co_3O_4 demonstrates the lowest gas sensitivity. Na et al. [12] observed a similar effect for nanocomposites consisting of Co_3O_4 nano islands immobilized on the surface of ZnO nanowires. Since NO_2 is an electron acceptor the sensor response is due to the localization of electrons on chemisorbed $NO_{2(ads)}^-$ particles:

$$NO_{2(gas)} + e^- \leftrightarrow NO_{2(ads)}^- \quad (5)$$

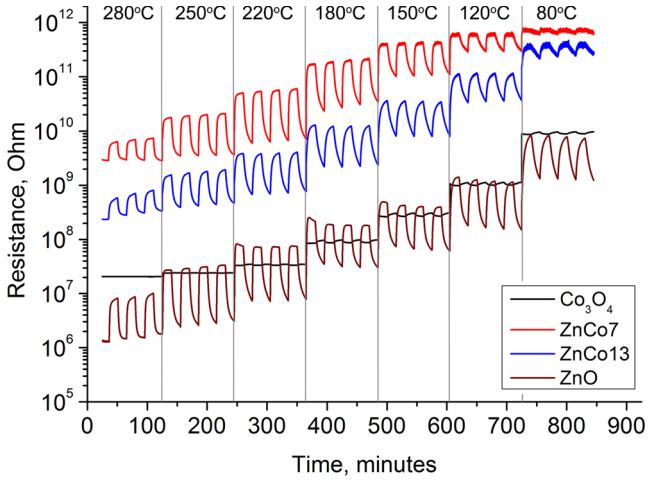

Fig. 9. Transient sensor response of ZnO-Co_3O_4 nanofibers to NO_2 (1 ppm, RH_{25} = 0 %) in the temperature range 80–280 °C.

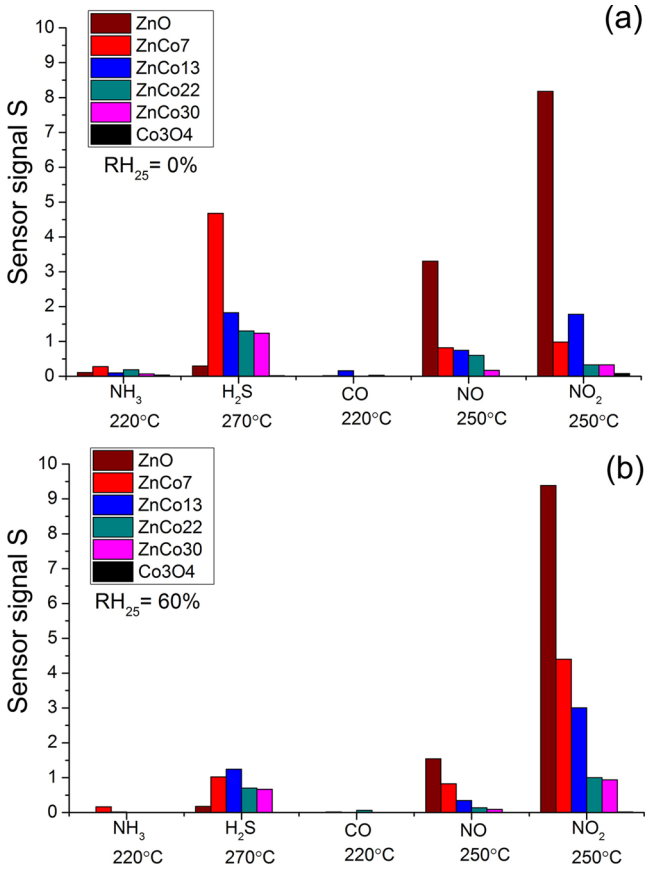

Fig. 10. Sensor signal of ZnO-Co_3O_4 nanofibers toward main air pollutants in (a) dry (RH_{25} = 0 %) and (b) wet (RH_{25} = 60 %) conditions. For the specific gas the values are presented for the temperature of maximal response.

In our previous work [42] it was shown that the sensor response to NO_2 increases with the electron concentration in ZnO-based materials. So, a decrease in the sensor sensitivity of nanocomposites toward NO_2 may be due to a decrease in the concentration of electrons capable of participating in the reaction (5). This assumption is confirmed by an increase in the materials resistance (Fig. 9), and a decrease in the concentration of chemisorbed oxygen $O^{\alpha-}_{\beta(ads)}$ (Fig. 7), which is also an acceptor gas (Eq. (1)).

In the case of H_2S detection the situation changes, the sensors based on nanocomposites ZnCo7 and ZnCo13 demonstrate the highest activity in dry and wet conditions, respectively (Fig. 10). The decrease in sensor resistance in the presence of H_2S (Fig. 11) is due to a decrease in the concentration of chemisorbed oxygen on the surface of *n*-type semiconductor oxides by reaction

$$\beta\bullet H_2S_{(gas)} + 3\bullet O^{\alpha-}_{\beta(ads)} \leftrightarrow \beta\bullet SO_{2(gas)} + \beta\bullet H_2O_{(gas)} + 3\alpha\bullet e^- \quad (6)$$

The dependences of the sensor signal of nanocomposites on the H_2S concentration (measured at 270 °C, Fig. 11) are linearized in double logarithmic coordinates (Fig. 12) corresponding to a power law $S \sim C^n_{H_2S}$. From these calibration curves the values of low detection limit (LDL) for H_2S were determined (Table 3). The value $\frac{R_{av}}{R_{av}-3\sigma}$, where R_{av} is the average resistance value and σ is the standard deviation of resistance in air, was taken as the minimum measurable response. In dry air, the nanocomposites ZnCo7, ZnCo13 and ZnCo30 are characterized by LDL values of 14–37 ppb. The increase in air humidity leads to a decrease in sensitivity to H_2S, however the nanocomposites are still characterized by lower LDL than ZnO.

To explain the effect of increased nanocomposites sensitivity to H_2S it is necessary to consider two models. Firstly, nanocomposites ZnCo13 and ZnCo30 contains $Zn_xCo_{3-x}O_4$ spinel particles that can be considered as a substituted Co_3O_4 solid solutions, where Zn^{2+} replace Co^{2+} cations in tetrahedral positions. These $Zn_xCo_{3-x}O_4$ complex oxides are also *p*-type semiconductors [43], which form $p-n$ heterojunctions at the *n*-type ZnO grain boundaries. This leads to the formation of an electrical barrier at the contacts between *n*-ZnO and *p*-$Zn_xCo_{3-x}O_4$ that is accompanied by a sharp increase in electrical resistance in pure air. It can be assumed that the high sensitivity to H_2S is caused by the interaction of H_2S with *p*-$Zn_xCo_{3-x}O_4$ leading to its transformation into metallic conductive cobalt sulfide [44,45]:

$$Zn_xCo_{3-x}O_4 + H_2S_{(gas)} + O_{2(gas)} \rightarrow xZnO + (3-x)CoO + SO_{2(gas)} + H_2O_{(gas)} \quad (7)$$

$$CoO + H_2S_{(gas)} \rightarrow CoS + H_2O_{(gas)} \quad (8)$$

This mechanism is similar to that previously established and proved for CuO/SnO_2 [46–48] and SnO_2/Co_3O_4 [44,45] nanocomposites. The transformation of *p*-$Zn_xCo_{3-x}O_4$ into metallic cobalt sulfide results in the removal of the $p-n$ heterojunctions and in a decrease in ZnO resistance. It should be noted that such removal of the barrier is only possible in the presence of H_2S. The interaction with other reducing gases (CO, H_2, NH_3) can lead only to the reduction of $Zn_xCo_{3-x}O_4$ to ZnO/CoO two phase system [29,49,50]. As cobalt (II) oxide CoO is also a *p*-type semiconductor, such transformation will not lead to the effective removal of the barrier. So, this mechanism of sensor response formation will not be realized.

On the other hand, as discussed above, the introduction of cobalt leads to a decrease in the acidity of the surface of nanocomposites compared with unmodified ZnO. This should enhance the adsorption of H_2S, which is an acidic gas, and therefore increase the sensor response of nanocomposites toward H_2S.

The values of response τ^{90}_{res} and recovery τ^{90}_{rec} time are presented in Table 4. Even though the absolute τ^{90}_{res} and τ^{90}_{rec} values are strongly dependent on the parameters of the testing system, they are useful to compare these characteristics of materials if the measurements are performed in identical conditions. The addition of a minimum amount of cobalt leads to a significant reduction in response time. With increasing cobalt concentration, the response time increases but remains less than that for ZnO. This trend has continued in the humid air. Generally, τ^{90}_{rec} is greater than τ^{90}_{res} and is less dependent on the composition of the sensor material and the air humidity, but the shortest τ^{90}_{rec} also corresponds to the ZnCo7 nanocomposite. These dynamic

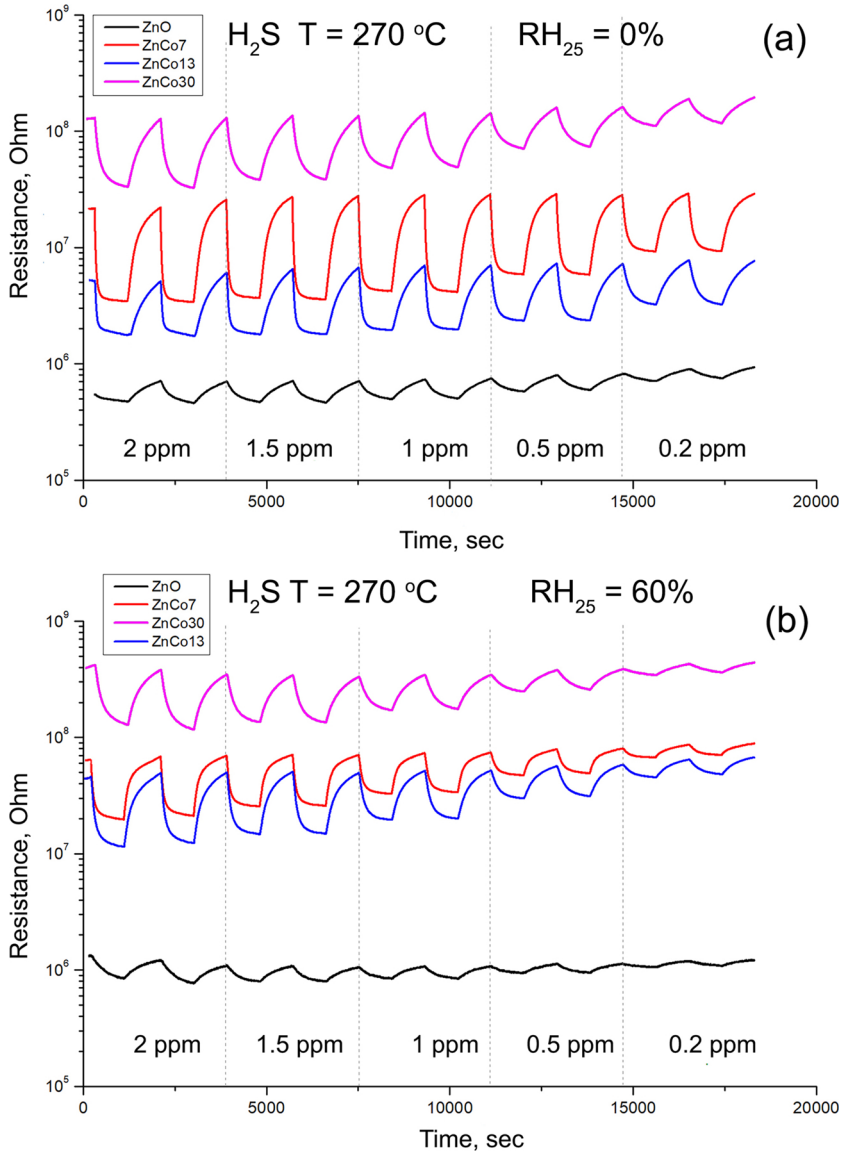

Fig. 11. Transient sensor response of ZnO-Co_3O_4 nanofibers to H_2S (0.2–2 ppm) at T = 270 °C in (a) dry (RH_{25} = 0 %) and (b) wet (RH_{25} = 60 %) conditions.

characteristics are determined by the kinetics of sequential and parallel processes: H_2S adsorption; surface reactions; diffusion of H_2S, oxygen and reaction products through the porous sensitive layer; desorption of the reaction products, which have different mechanisms and energetic characteristics. It can be assumed that the reduction in τ_{res}^{90} and τ_{rec}^{90} for nanocomposites is due to the formation of a hollow tubular structure of nanofibers (Fig. 2), which provides additional opportunities for the transport of gas molecules through the sensitive layer.

To determine the long-term stability of the sensor signal, continuous measurements were carried out for 14 days. The resistance of ZnCo7 and ZnCo13 nanocomposites was measured at T = 270 °C with the introduction of 1 ppm H_2S in dry and humid air. The results are shown in Fig. 13 as the value of the sensor signal depending on the day of measurement. Both sensors demonstrated satisfactory response stability (within 5 %). It should be noted that the value of the sensor response of the ZnCo13 nanocomposite weakly decreases with increasing relative humidity up to RH_{25} = 60 %.

4. Conclusions

ZnO – Co_3O_4 nanocomposites were obtained by co-electrospinning process from single solutions of different cobalt content [Co]/([Co] + [Zn]) = 7–30 wt. %. The joint presence of zinc and cobalt salts in the initial solution leads to the formation of hollow tubes that are not formed in the cases of the individual oxides. It is found that cobalt is present in samples in both oxidation states Co^{2+} and Co^{3+}. The $Zn_xCo_{3-x}O_4$ and $Zn_{1-y}Co_yO$ crystalline phases were detected by X-ray diffraction. The walls of the tubular structures are formed by agglomerated nanoparticles of the $Zn_{1-y}Co_yO$ solid solution, while nanoparticles with higher cobalt content ($Zn_xCo_{3-x}O_4$ solid solution) with a spinel structure are present on the surface of the wall. The sensor properties of individual oxides and nanocomposites have been measured towards main air pollutants: NO, NO_2, NH_3, CO and H_2S in dry and humid air. The composition of the fibers has a key effect on the selectivity of the sensors. The gas sensors fabricated from bare ZnO demonstrate high selective sensitivity to nitrogen oxides NO, NO_2. The sensors based on ZnO-Co_3O_4 composites have selective sensitivity towards H_2S. The

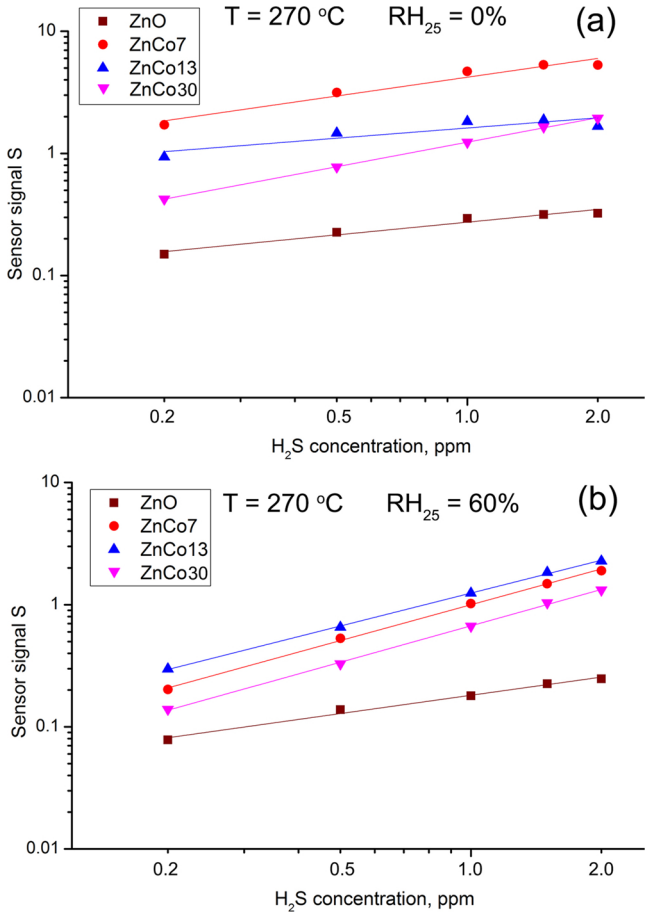

Fig. 12. Calibration curves for H_2S detection at T = 270 °C in (a) dry (RH_{25} = 0 %) and (b) wet (RH_{25} = 60 %) conditions.

Table 3
H_2S detection limit (LDL) for sensors based on ZnO, ZnCo7, ZnCo13 and ZnCo30 nanofibers.

Sample	LDL, ppb	
	RH_{25} = 0%	RH_{25} = 60%
ZnO	610	330
ZnCo7	14	260
ZnCo13	37	260
ZnCo30	23	330

Table 4
Response τ_{res}^{90} and recovery τ_{rec}^{90} time (270 °C, 1 ppm H_2S).

	τ_{res}^{90}, sec		τ_{rec}^{90}, sec	
	RH_{25} = 0%	RH_{25} = 60%	RH_{25} = 0%	RH_{25} = 60%
ZnO	618	635	788	774
ZnCo7	85	218	705	644
ZnCo13	143	286	777	700
ZnCo22	390	410	780	733
ZnCo33	409	498	782	752

sensitivity of ZnCo13 nanocomposite to H_2S is practically not reduced with a significant increase in air humidity up to RH_{25} = 60 %. The increase of sensor signal of ZnO-Co_3O_4 nanocomposites compared with ZnO nanofibers may be caused by selective interaction of H_2S with cobalt containing oxides on the surface of ZnO nanofibers resulting in transformation of *p*-type cobalt oxides into cobalt sulfides with metallic

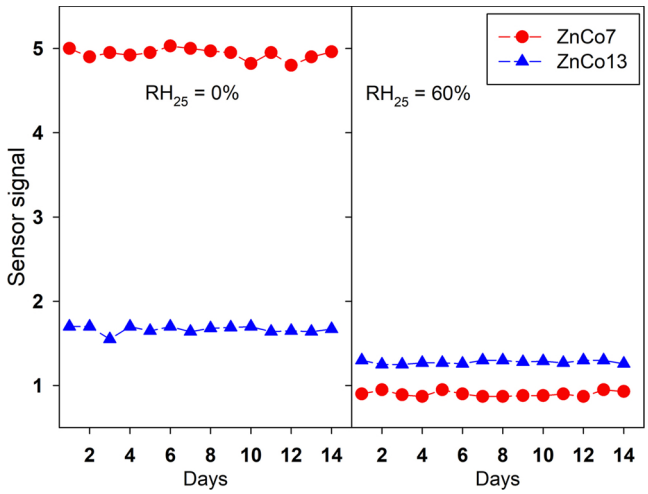

Fig. 13. Stability of the sensor response of ZnCo7 and ZnCo13 nanocomposites toward 1 ppm H_2S in dry and humid air, continuous measurements were carried out for 14 days.

conductivity, or by a decrease in the acidity of the ZnO surface when cobalt is added. The observed reduction in response and recovery time of nanocomposites compared with unmodified ZnO may be due to the formation of a tubular structure providing additional opportunities for the transport of gas molecules through the sensitive layer.

Declaration of competing interest

The authors declare that they have no known competing financial interests or personal relationships that could have appeared to influence the work reported in this paper.

Acknowledgements

This work was supported by RFBR grants No. 18-03-00091 and No. 18-03-00580.

Appendix A. Supplementary data

Supplementary material related to this article can be found, in the online version, at doi:https://doi.org/10.1016/j.snb.2019.127624.

References

[1] G. Korotcenkov, B.K. Cho, Metal oxide composites in conductometric gas sensors: achievements and challenges, Sens. Actuators B Chem. 244 (2017) 182–210, https://doi.org/10.1016/j.snb.2016.12.117.
[2] D.R. Miller, S.A. Akbar, P.A. Morris, Nanoscale metal oxide-based heterojunctions for gas sensing: a review, Sens. Actuators B Chem. 204 (2014) 250–272, https://doi.org/10.1016/j.snb.2014.07.074.
[3] V.V. Krivetskiy, M.N. Rumyantseva, A.M. Gaskov, Chemical modification of nanocrystalline tin dioxide for selective gas sensors, Russ. Chem. Rev. 82 (2013) 917–941, https://doi.org/10.1070/RC2013v082n10ABEH004366.
[4] A.V. Marikutsa, N.A. Vorobyeva, M.N. Rumyantseva, A.M. Gaskov, Active sites on the surface of nanocrystalline semiconductor oxides ZnO and SnO_2 and gas sensitivity, Russ. Chem. Bull. 66 (2017) 1728–1764, https://doi.org/10.1007/s11172-017-1949-7.
[5] L. Xu, Z. Shuhai, L.J. Song, J. Chen, B. Dong, H. Song, NiO@ZnO heterostructured nanotubes: coelectrospinning fabrication, characterization, and highly enhanced gas sensing properties, Inorg. Chem. 51 (2012) 7733–7740, https://doi.org/10.1021/ic300749a.
[6] S. Bai, H. Luo, A. Chen, D. Li, SnO_2@Co_3O_4 p-n heterostructures fabricated by electrospinning and mechanism analysis enhanced aceton sensing, RSC Adv. 4 (2014) 62862–62868, https://doi.org/10.1039/c4ra09766a.
[7] C.W. Na, H.-S. Woo, I.-D. Kim, J.-H. Lee, Selective detection of NO_2 and C_2H_5OH using a Co_3O_4-decorated ZnO nanowire network sensor, Chem. Commun. (Camb.) 47 (2011), https://doi.org/10.1039/C0CC05256F 5148–.
[8] D. Bekermann, A. Gasparotto, D. Barreca, C. Maccato, E. Comini, C. Sada, G. Sberveglieri, A. Devi, R.A. Fischer, Co_3O_4/ZnO nanocomposites: from plasma synthesis to gas sensing applications, Appl. Mater. Interfaces 4 (2012) 928–934, https://doi.org/10.1021/am201591w.

[9] Y. Liu, G. Zhu, J. Chen, H. Xu, X. Shen, A. Yuan, Co_3O_4/ZnO nanocomposites for gas-sensing applications, Appl. Surf. Sci. 265 (2013) 379–384, https://doi.org/10.1016/j.apsusc.2012.11.016.

[10] D. Ju, H. Xu, Z. Qiu, J. Guo, J. Zhang, B. Cao, Highly sensitive and selective triethylamine-sensing properties of nanosheets directly grown on ceramic tube by forming NiO/ZnO PN heterojunction, Sens. Actuators B Chem. 200 (2014) 288–296, https://doi.org/10.1016/j.snb.2014.04.029.

[11] M.A. Kanjwal, F.A. Sheikh, N.A.M. Barakat, I.S. Chronakis, H.Y. Kim, Co_3O_4–ZnO hierarchical nanostructures by electrospinning and hydrothermal methods, Appl. Surf. Sci. 257 (2011) 7975–7981, https://doi.org/10.1016/j.apsusc.2011.04.034.

[12] Ch.W. Na, H.-S. Woo, I.-D. Kim, J.-H. Lee, Selective detection of NO_2 and C_2H_5OH using a Co_3O_4-decorated ZnO nanowire network sensor, Chem. Commun. (Camb.) 47 (2011) 5148–5150, https://doi.org/10.1039/c0cc05256f.

[13] Y. Liu, G. Zhu, J. Chen, H. Xu, X. Shen, A. Yuan, Co_3O_4/ZnO nanocomposites for gas-sensing applications, Appl. Surf. Sci. 265 (2013) 379–384 https://10.1016/j.apsusc.2012.11.016.

[14] L. Zhang, X. Jing, J. Liu, J. Wang, Y. Sun, Facile synthesis of mesoporous ZnO/Co_3O_4 microspheres with enhanced gas-sensing for ethanol, Sens. Actuators B Chem. 221 (2015) 1492–1498, https://doi.org/10.1016/j.snb.2015.07.113.

[15] Y. Xiong, W. Xu, Z. Zhu, Q. Xue, W. Lu, D. Ding, L. Zhu, ZIF-derived porous ZnO-Co_3O_4 hollow polyhedrons heterostructure with highly enhanced ethanol detection performance, Sens. Actuators B Chem. 253 (2017) 523–532, https://doi.org/10.1016/j.snb.2017.06.169.

[16] Sh. Bai, J. Guo, X. Shu, X. Xiang, R. Luo, D. Li, A. Chen, Ch.Ch. Liu, Surface functionalization of Co_3O_4 hollow spheres with ZnO nanoparticles for modulating sensing properties of formaldehyde, Sens. Actuators B Chem. 245 (2017) 359–368, https://doi.org/10.1016/j.snb.2017.01.102.

[17] R.S. Andre, J.C. Pereira, L.A. Mercante, D. Locilento, L.H.C. Mattoso, D.S. Correa, ZnO-Co_3O_4heterostructure electrospun nanofibers modified with poly(sodium 4-styrenesulfonate): Evaluation of humidity sensing properties, J. Alloys. Compd. 767 (2018) 1022–1029, https://doi.org/10.1016/j.jallcom.2018.07.132.

[18] X. Gao, F. Li, R. Wang, T. Zhang, A formaldehyde sensor: significant role of p-n heterojunction in gas-sensitive core-shell nanofibers, Sens. Actuators B Chem. 258 (2018) 1230–1241, https://doi.org/10.1016/j.snb.2017.11.088.

[19] B. Li, J. Liu, Q. Liu, R. Chen, H. Zhang, J. Yu, D. Song, J. Li, M. Zhang, J. Wang, Core-shell structure of ZnO/Co_3O_4 composites derived from bimetallic-organic frameworks with superior sensing performance for ethanol gas, Appl. Surf. Sci. 475 (2019) 700–709, https://doi.org/10.1016/j.apsusc.2018.12.284.

[20] D. Zhang, Zh. Yang, Zh. Wu, G. Dong, Metal-organic frameworks-derived hollow zinc oxide/cobalt oxide nanoheterostructure for highly sensitive acetone sensing, Sens. Actuators B Chem. 283 (2019) 42–51, https://doi.org/10.1016/j.snb.2018.11.133.

[21] Ya. Li, N. Luo, G. Sun, B. Zhang, H. Jin, L. Lin, H. Bala, J. Cao, Zh. Zhang, Ya. Wang, Synthesis of porous nanosheets-assembled ZnO/$ZnCo_2O_4$ hierarchical structure for TEA detection, Sens. Actuators B Chem. 287 (2019) 199–208, https://doi.org/10.1016/j.snb.2019.02.055.

[22] Z. Zhang, Efficiency enhancement of ZnO/Cu_2O solar cells with well oriented and micrometer grain sized Cu_2O films, Appl. Phys. Lett. 112 (2018) 042106, , https://doi.org/10.1063/1.5017002.

[23] Z. Zhang, X. Zeng, J. Du, M. Wang, X. Tang, Femtosecond laser direct writing of microholes on roughened ZnO for output power enhancement of InGaN light-emitting diodes, Chin. Opt. Lett. 41 (2016) 3463–3466, https://doi.org/10.1364/OL.41.003463.

[24] C. Li, Z. Znag, C. Han, Z. Hu, X. Tang, J. Du, Y. Leng, K. Sun, Highly compact CsPbBr3 perovskite thin films decorated by ZnO nanoparticles for enhanced random lasing, Nano Energy 40 (2017) 195–202, https://doi.org/10.1016/j.nanoen.2017.08.013.

[25] Z. Zhang, X. Tang, Enhanced fluorescence imaging performance of hydrophobic colloidal nanoparticles by a facile method, J. Alloys. Compd. 619 (2015) 98–101, https://doi.org/10.1016/j.jallcom.2014.09.072.

[26] Ü. Özgür, Ya.I. Alivov, C. Liu, A. Teke, M.A. Reshchikov, S. Doğan, V. Avrutin, S.-J. Cho, H. Morkoç, A comprehensive review of ZnO materials and devices, J. Appl. Phys. 98 (2005) 041301, , https://doi.org/10.1063/1.1992666.

[27] J.M. Xu, J.P. Cheng, The advances of Co_3O_4 as gas sensing materials: a review, J. Alloys. Compd. 686 (2016) 753–768, https://doi.org/10.1016/j.jallcom.2016.06.086.

[28] L. Simonot, F. Garin, G. Maire, A comparative study of $LaCoO_3$, Co_3O_4 and $LaCoO_3$-Co_3O_4. Preparation, characterization and catalytic properties for the oxidation of CO, Appl. Catal. B 11 (1997) 167–179, https://doi.org/10.1016/S0926-3373(96)00046-X.

[29] S. Royer, D. Duprez, Catalytic oxidation of carbon monoxide over transition metal oxides, ChemCatChem 3 (2011) 24–65, https://doi.org/10.1002/cctc.201000378.

[30] Z. Li, C. Wang, One-Dimensional Nanostructures. Electrospinning Technique and Unique Nanofibers, Springer Briefs in Materials, Heidelberg New York Dordrecht London, 2019, p. p.134, https://doi.org/10.1007/978-3-642-36427-3.

[31] K. Mondal, A. Sharma, Recent advances in electrospun metal oxide nanofiber based interfaces for electrochemical biosensing, RSC Adv. 6 (2016) 94595–94616, https://doi.org/10.1039/c6ra21477k.

[32] Zh. Jiang, Y. Zhao, P. Yang, Formation of MFe_2O_4 (M = Co, Mn, Ni) 1D nanostructures towards rapid removal of pollutants, Mater. Chem. Phys. 214 (2018) 1–7, https://doi.org/10.1016/j.matchemphys.2018.04.066.

[33] T. Dong, P. Wang, P. Yang, Synthesis of magnetic Ag_3PO_4/Ag/$NiFe_2O_4$ composites towards super photocatalysis and magnetic separation, Int. J. Hydrogen Energy 43 (2018) 20607–20615, https://doi.org/10.1016/j.ijhydene.2018.09.079.

[34] K. Lee, A. Mazare, P. Schmuki, One-dimensional titanium dioxide nanomaterials: nanotubes, Chem. Rev. 114 (2014) 9385–9454, https://doi.org/10.1021/cr500061m.

[35] D.-X. Ju, H.-Y. Xu, Z.-W. Qiu, Z.-C. Zhang, Q. Xi, J. Zhang, J.-Q. Wang, B.-Q. Cao, Near room temperature, Fast-Response, and highly sensitive triethylamine sensor assembled with Au-Loaded ZnO/SnO_2 core-shell nanorods on flat alumina

[36] X. Song, L. Li, X. Chen, Q. Xu, B. Song, Z. Pan, Y. Liu, F. Juan, F. Xu, B. Cao, Enhanced triethylamine sensing performance of α-Fe_2O_3 nanoparticle/ZnO nanorod heterostructures, Sens. Actuators B Chem. 298 (2019) 12697, https://doi.org/10.1016/j.snb.2019.126917.

[37] M.N. Rumyantseva, E.A. Makeeva, S.M. Badalyan, A.A. Zhukova, A.M. Gaskov, Nanocrystalline SnO_2 and In_2O_3 as materials for gas sensors: the relationship between microstructure and oxygen chemisorption, Thin Solid Films 518 (2009) 1283–1288, https://doi.org/10.1016/j.tsf.2009.07.201.

[38] N. Bârsan, U. Weimar, Conduction model of metal oxide gas sensors, J. Electroceram. 7 (2001) 143–167, https://doi.org/10.1023/A:1014405811371.

[39] C.C. Li, Z.F. Du, L.M. Li, H.C. Yu, Q. Wan, T.H. Wang, Surface-depletion controlled gas sensing of ZnO nanorods grown at room temperature, Appl. Phys. Lett. 91 (2007) 032101, , https://doi.org/10.1063/1.2752541.

[40] E. Wograt, N. Hongsith, D. Wongratanaphisan, A. Gardchareon, S. Choopun, Control of depletion layer width via amount of AuNPs for sensor response enhancement in ZnO nanostructure sensor, Sens. Actuators B Chem. 171-172 (2012) 230–237, https://doi.org/10.1016/j.snb.2012.03.050.

[41] J. Portier, G. Campet, J. Etourneau, M.C.R. Shastry, B. Tanguy, A simple approach to materials design: role played by an ionic-covalent parameter based on polarizing power and electronegativity, J. Alloys. Compd. 209 (1994) 59–64, https://doi.org/10.1016/0925-8388(94)91076-6.

[42] N. Vorobyeva, M. Rumyantseva, D. Filatova, E. Konstantinova, D. Grishina, A. Abakumov, S. Turner, A. Gaskov, Nanocrystalline ZnO(Ga): paramagnetic centers, surface acidity and gas sensor properties, Sens. Actuators B Chem. 182 (2013) 555–564, https://doi.org/10.1016/j.snb.2013.03.068.

[43] S.M. McCullough, C.J. Flynn, C.C. Mercado, A.J. Nozik, J.F. Cahoon, Compositionally-tunable mechanochemical synthesis of $Zn_xCo_{3-x}O_4$ nanoparticles for mesoporous p-Type photocathodes, J. Mater. Chem. A Mater. Energy Sustain. 3 (2015) 21990–21994, https://doi.org/10.1039/C5TA07491F.

[44] S.A. Vladimirova, M.N. Rumyantseva, D.G. Filatova, A.S. Chizhov, N.O. Khmelevsky, E.A. Konstantinova, V.F. Kozlovsky, A.V. Marchevsky, O.M. Karakulina, J. Hadermann, A.M. Gaskov, Cobalt location in p-CoO_x/n-SnO_2 nanocomposites: correlation with gas sensor performances, J. Alloys. Compd. 721 (2017) 249–260, https://doi.org/10.1016/j.jallcom.2017.05.332.

[45] M.N. Rumyantseva, S.A. Vladimirova, N.A. Vorobyeva, I. Giebelhaus, S. Mathur, A.S. Chizhov, N.O. Khmelevsky, A.Yu. Aksenenko, V.F. Kozlovsky, O.M. Karakulina, J. Hadermann, A.M. Abakumov, A.M. Gaskov, p-CoO_x/n-SnO_2 nanostructures: New highly selective materials for H_2S detection, Sens. Actuators B Chem. 255 (2018) 564–571, https://doi.org/10.1016/j.snb.2017.08.096.

[46] J. Tamaki, T. Maekawa, N. Miura, N. Yamazoe, CuO – SnO_2 element of highly sensitive and selective detection of H_2S, Sens. Actuators B Chem. 9 (1992) 197–203, https://doi.org/10.1016/0925-4005(92)80216-K.

[47] M. Boulova, A. Galerie, A. Gaskov, G. Lucazeau, Reactivity of SnO_2-CuO nanocrystalline materials with H_{2S}: a coupled electrical and Raman spectroscopic study, Sens. Actuators B Chem. 71 (2000) 134–139, https://doi.org/10.1016/S0925-4005(00)00598-0.

[48] L.A. Patil, D.R. Patil, Heterocontact type CuO-modified SnO_2 sensor for the detection of a ppm level H_2S gas at room temperature, Sens. Actuators B Chem. 120 (2006) 316–323, https://doi.org/10.1016/j.snb.2006.02.022.

[49] G. Busca, R. Guidetti, V. Lorenzelli, Fourier-transform infrared study of the surface properties of cobalt oxides, J. Chem. Soc. Faraday Trans. 86 (1990) 989–994, https://doi.org/10.1039/FT9908600989.

[50] K. Schmidt-Szałowski, K. Krawczyk, J. Petryk, The properties of cobalt oxide catalyst for ammonia oxidation, Appl. Catal. A Gen. 175 (1998) 147–157, https://doi.org/10.1016/S0926-860X(98)00206-3.